Article

Fractional Active Disturbance Rejection Positioning and Docking Control of Remotely Operated Vehicles: Analysis and Experimental Validation

Weidong Liu, Liwei Guo [ID]**, Le Li *** [ID]**, Jingming Xu and Guanghao Yang**

School of Marine Science and Technology, Northwestern Polytechnical University, Xi'an 710072, China;
liuwd@nwpu.edu.cn (W.L.); 2019100504@mail.nwpu.edu.cn (L.G.); 2018260584@mail.nwpu.edu.cn (J.X.);
2022260761@mail.nwpu.edu.cn (G.Y.)
* Correspondence: leli@nwpu.edu.cn

Abstract: In this paper, a fractional active disturbance rejection control (FADRC) scheme is proposed for remotely operated vehicles (ROVs) to enhance high-precision positioning and docking control in the presence of ocean current disturbances and model uncertainties. The scheme comprises a double closed-loop fractional-order $PI^\lambda D^\mu$ controller (DFOPID) and a model-assisted finite-time sliding-mode extended state observer (MFSESO). Among them, DFOPID effectively compensates for non-matching disturbances, while its fractional-order term enhances the dynamic performance and steady-state accuracy of the system. MFSESO contributes to enhancing the estimation accuracy through the integration of sliding-mode technology and model information, ensuring the finite-time convergence of observation errors. Numerical simulations and pool experiments have shown that the proposed control scheme can effectively resist disturbances and successfully complete high-precision tasks in the absence of an accurate model. This underscores the independence of this control scheme on accurate model data of an operational ROV. Meanwhile, it also has the advantages of a simple structure and easy parameter tuning. The FADRC scheme presented in this paper holds practical significance and can serve as a valuable reference for applications involving ROVs.

Keywords: fractional active disturbance rejection control (FADRC); double closed-loop fractional-order $PI^\lambda D^\mu$ controller (DFOPID); model-assisted finite-time sliding-mode extended state observer (MFSESO); remotely operated vehicle (ROV); remotely operated vehicle (ROV)

1. Introduction

ROVs play a significant role in the realm of underwater robotics due to their cost-effectiveness, safety features, and robust operational capacities. These devices have found extensive application in diverse fields, including marine environmental surveillance, seabed topography assessments, underwater search-and-rescue operations, marine resource collection, etc. [1]. The above tasks require ROVs to have excellent control performance. This enables them to carry out high-precision docking operations with underwater devices to facilitate ROV submarine operations, underwater recovery, underwater device data backhaul, fault inspection, and power supply replacement, among other functions. However, challenges arise in achieving high-precision control of ROVs due to difficulties in accurately acquiring the ROV model and external disturbances like ocean currents in the marine environment.

In recent years, many researchers have dedicated themselves to studying the positioning and docking control of underwater vehicles. Hiroshi proposed the linear parameter-varying model predictive control (MPC) method for the docking operation, and simulation results show that this control method can effectively handle the influence of various ocean current disturbances [2]. Ohrem designed a nonlinear robust adaptive backstepping controller to ensure the dynamic positioning of ROVs in environments with model uncertainty

and unknown disturbances. Extensive field trials in aquaculture applications have been successfully conducted using this controller [3]. Xie proposed a 3D mobile docking control method based on backstepping sliding mode control (SMC), which efficiently completed the underactuated autonomous underwater vehicle (AUV) mobile docking task in the presence of unknown ocean current disturbances [4]. Wu proposed a hybrid proportional integral derivative (PID) controller for a work-class ROV to achieve high-performance maneuvering [5]. Song developed an improved model-based PI robust controller using a nominal model for the precise positioning control of a hexagonal multi-vector propulsion ROV with communication time-delay constraints [6]. Li utilized a linear ADRC scheme that combines a reduced-order extended state observer and approximate time-optimal control; simulation results confirmed its effective control performance [7]. Zhang developed a model-free docking controller using deep reinforcement learning to complete three-dimensional docking tasks under disturbances [8]. Wang proposed a two-step adaptive control method to solve the planar-type docking problem, seamlessly combining horizontal dynamic positioning and visual servo docking [9].

From the above discussion, it can be seen that the control methods for the positioning and docking of underwater vehicles can be roughly divided into model-based control paradigms, such as SMC, MPC, and backstepping, and data-based control paradigms, such as PID. Model-based control paradigms are mathematically rigorous and demonstrate excellent theoretical control performance, but their application is limited. The key point is that the mathematical model of the system object may not be entirely accurate in most scenarios. Operational ROVs are often subject to unknown disturbances from umbilical cables and ocean currents. Additionally, depending on the operation's content, ROVs often require the replacement of manipulators and other work tools, making it more difficult to obtain an accurate dynamic model. A data-based control paradigm has a simple structure, allows easy parameter tuning, and is economical and practical. Employing data-based control paradigms is still the most widely used strategy in control. Traditional PID control is based on feedback error correction, which inherently exhibits a hysteresis effect and a limited anti-disturbance capability [10]. This characteristic makes it less ideal for control scenarios demanding high accuracy. Therefore, the proposal of a control paradigm that can combine the advantages of both is urgently needed.

As a new nonlinear robust control technique, ADRC can unify the above two control paradigms by incorporating the nominal model of the system in the observer design. Nonlinear ADRC mainly consists of a tracking differentiator, an extended state observer, and a nonlinear-state error feedback control law. The core idea is to consider the nominal model or integral series type of the system as the standard type. Simultaneously, the components of the system dynamics that differ from the standard type, such as system uncertainty and external disturbances, are considered as total disturbances. An observer is used to estimate the total disturbance in real time and eliminate it. Finally, the error is eradicated through the application of a nonlinear-state error feedback control law [11]. This technique exhibits good robustness, gives a fast response, has a strong anti-disturbance ability, and does not rely on the accurate mathematical model of the controlled object. It can be used when the model is completely unknown or when some information about the model is known. In light of the limitations of nonlinear ADRC due to its complex structure, numerous control parameters, and challenging tuning process, the linear ADRC method simplifies the structure by converting all controllers and extended state observers into a linear form. This approach allows for individual adjustments to be made to the controller bandwidth and observer bandwidth, thereby enhancing the effectiveness of ADRC in engineering applications [12]. Therefore, ADRC has attracted the attention of many researchers in the field of underwater vehicle motion control. Liu introduced the ADRC technique to achieve depth control for autonomous underwater vehicle (AUV). He utilized an improved speed saturation tracking differentiator to enhance the controller's adaptability to control instructions [13]. Wang utilized ADRC-based dynamic controllers in AUV formations to ensure that followers and leaders consistently maintained the desired

distance [14]. Gao proposed an ADRC method based on dynamic inversion to achieve motion control of underwater vehicle-manipulator systems (UVMSs) [15]. Zhou designed a robust dynamic heading-tracking control method based on an improved ADRC method and an enhanced anti-convolution compensator. Zhou's study confirmed that the proposed control method can achieve high accuracy in heading tracking [16]. Li utilized ADRC technology to develop a tandem-level ADRC controller for a water–air multi-rotor vehicle. Additionally, Li introduced the particle swarm optimization (PSO) algorithm to efficiently adjust the controller parameters, ensuring that the controller meets the performance criteria in challenging underwater environments [17]. Liu proposed a depth-tracking method for underactuated AUVs, using an ADRC framework to compensate for the complex unknown pitch dynamics by approximating them into an integral series; the effectiveness and strong disturbance rejection capabilities of the proposed method were verified with field comparison experiments [18]. Nevertheless, many of the research studies referenced here fail to consider the effects of non-matching disturbances, while the conventional ADRC's PID controller encounters challenges in achieving precise control performance at a high level.

Fractional calculus is an extension of traditional calculus that describes the fractal dimension of a space. Podlubny first applied the concept of fractional order to controller design and proposed the fractional-order $PI^\lambda D^\mu$ controller [19]. Compared with the integer PID controller, a fractional-order $PI^\lambda D^\mu$ controller has two additional adjustable parameters, namely integral order λ and differential order μ, which can obtain more flexible amplitude–phase characteristics, so as to achieve high-precision and fast-response control performance. At the same time, the fractional-order $PI^\lambda D^\mu$ controller exhibits greater adaptability to parameter changes in the controlled object of the system. When the parameter of the controlled object changes within a certain allowable range, the system characteristics remain basically unchanged, indicating that the fractional-order $PI^\lambda D^\mu$ controller exhibits strong robustness. Fractional-order $PI^\lambda D^\mu$ controllers have been extensively researched in the field of underwater vehicle control. For AUV heading control, Liu designed a robust fractional-order $PI^\lambda D^\mu$ controller that effectively resists parametric uncertainty and demonstrates good robustness and dynamic performance [20]. Zhu proposed a fractional-order control method based on fuzzy logic and achieved good dynamic and steady-state characteristics through an AUV depth control simulation [21]. Li proposed an adaptive fractional-order non-singular terminal sliding-mode trajectory-tracking controller for an underwater robot, which can achieve fast switching gain, avoid over-tuning, and effectively improve the accuracy and robustness [22]. Zhang proposed a nonlinear fractional-order PD^μ controller based on saturation, which exhibits good dynamic performance and robustness. Additionally, it offers the advantages of a simple structure and easy implementation [23]. Cui designed a single-input fractional fuzzy logic controller for an unmanned underwater vehicle (UUV) motion control system. Simulation results demonstrate that Cui's control algorithm exhibits good stability and transient performance [24]. Liu proposed a fractional-order PI^λ controller for UUVs that guarantees both frequency-domain and time-domain behavior, offering greater flexibility in enhancing the system robustness and transient performance [25]. Hansan designed an adaptive neural network with a nonlinear fractional-order $PI^\lambda D^\mu$ controller for the path-tracking problem of underwater vehicles [26]. ROV positioning and docking operations have high requirements for the robustness and dynamic performance of the control system. The application of fractional-order $PI^\lambda D^\mu$ control in this task has not been reported. Simultaneously, the faster dynamic response of fractional-order $PI^\lambda D^\mu$ can more effectively reduce the observation error of the observer in ADRC. Therefore, FADRC can combine the advantages of ADRC and fractional-order $PI^\lambda D^\mu$ control, resulting in superior control performance. At the same time, it also ensures the simple structure of the controller and is easy to implement in practice.

Aiming to address the challenges of high-precision positioning and docking control of ROVs under ocean current disturbances and model uncertainties, this paper proposes an FADRC scheme. The proposed scheme consists of a double closed-loop fractional-order

PI$^\lambda$D$^\mu$ controller and a model-assisted finite-time sliding-mode extended state observer. Regarding the existing research on ADRC for ROVs, compared to previous studies focusing on improving the observer and the tracking differentiator algorithms themselves, this paper innovatively introduces a fractional-order PI$^\lambda$D$^\mu$ controller and adds the observation of the velocity term in the kinematic channel, enhancing the robustness of high-precision ROV operations and effectively reducing the impact of matching and non-matching disturbances. Its main contributions are as follows:

1. In order to better compensate for the non-matching disturbance caused by ocean currents on the kinematics of ROVs and to generate a smooth and ideal transition process, a double closed-loop control structure composed of a position control loop and a velocity control loop is adopted. In order to effectively enhance the robustness and dynamic performance of high-precision positioning and docking control of ROVs, a fractional-order PI$^\lambda$D$^\mu$ controller is introduced in the velocity control loop. Its integral and differential orders can be arbitrarily selected, providing more flexibility than an integer-order controller. At the same time, the fractional-order controller exhibits strong robustness to changes in the parameters of the controlled object;

2. The ROV nominal model is integrated into the extended state observer, and a model-assisted finite-time sliding-mode extended state observer is designed to eliminate the dependence on the accurate model. A Lyapunov function is formulated to demonstrate the finite-time convergence of the observation error. The introduction of this nominal model can effectively reduce the gain of the observer and improve the estimation accuracy. The sliding-mode technology can enhance the robustness of the observer, accelerate error convergence [27], and further improve the performance of the ROV positioning and docking control;

3. Numerical simulations and pool experiments are conducted on the ROV to perform positioning and docking tasks in the presence of ocean current disturbances and model uncertainties. Compared to the currently most widely used PID and ADRC method, the control scheme proposed in this paper has advantages in high-precision operations.

The remainder of this paper is arranged as follows: Section 2 introduces the kinematic and dynamic models of an operational ROV in the presence of ocean currents and describes the control objectives. Section 3 introduces the FADRC scheme, discusses the double closed-loop fractional-order PI$^\lambda$D$^\mu$ controller, and elaborates on the model-assisted finite-time sliding-mode extended state observer. Section 4 elaborates on numerical simulations and pool experiments, which verify the advantages of the proposed scheme. The conclusions are provided in Section 5.

2. ROV Modeling and Problem Formulation

This section provides a detailed analysis of the kinematics and dynamics of an operational ROV in an ocean current environment. It also outlines the control objectives for positioning and docking.

2.1. ROV Kinematics

As shown in Figure 1, the inertial coordinate system {I} and the body coordinate system {B} are established to describe the ROV's spatial motion. Among them, $\boldsymbol{\eta} = [x, y, z, \phi, \theta, \psi]^T \in \mathbb{R}^6$ represents the position and direction angle of the ROV in the inertial coordinate system {I} and the body coordinate system {B}, and $\boldsymbol{v} = [u, v, w, p, q, r]^T \in \mathbb{R}^6$ represents the linear velocity and angular velocity of the ROV under the body coordinate system {B}, while $\boldsymbol{\tau} = [X, Y, Z, K, M, N]^T \in \mathbb{R}^6$ represents the external force and moment acting on the ROV under the body coordinate system {B}. The kinematic model of the ROV considering the current field is

$$\dot{\boldsymbol{\eta}} = \boldsymbol{J}(\boldsymbol{\eta})\boldsymbol{v}_r + \boldsymbol{v}_f \qquad (1)$$

In Equation (1), $J(\eta) \in \mathbb{R}^{6 \times 6}$ represents the velocity transformation matrix of the ROV between the inertial coordinate system and the body coordinate system, and $v_r \in \mathbb{R}^6$ represents the velocity vector of the ROV relative to the ocean current under the body coordinate system {B}, while $v_f \in \mathbb{R}^6$ represents the velocity vector of the ocean current under the inertial coordinate system {I}. The relationship between v_r, v_f, and v is described as follows:

$$\begin{cases} \dot{\eta} = J(\eta)v_r + v_f \\ v = v_r + v_c \\ v_f = J(\eta)v_c \end{cases} \tag{2}$$

$v_c \in \mathbb{R}^6$ represents the velocity vector of the ocean current in the body coordinate system {B}.
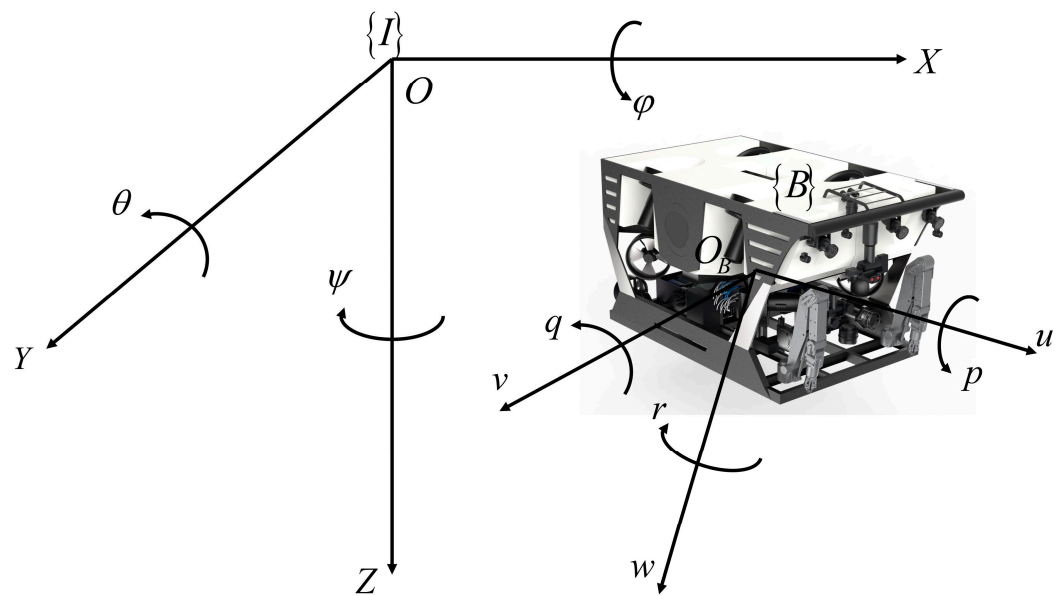
Figure 1. The inertial coordinate system {I} and the body coordinate system {B}.

ROVs can obtain v_r using their own inertial guidance equipment, but it is usually difficult to obtain v_f. When an ROV performs high-precision tasks, v_f needs to be estimated and compensated. Since v_f and $\dot{v}_f$ satisfy the law of conservation of fluid energy [28], the following reasonable assumption can be made:

Assumption 1. *The ocean current velocity v_f and its derivative $\dot{v}_f$ satisfy the bounded condition $\|v_f\|_2 \leq k_f$, $\|\dot{v}_f\|_2 \leq k_{df}$, where $\|\cdot\|_2$ represents the Euclidean norm. k_f and k_{df} are definite constants.*

2.2. ROV Dynamics

The dynamic model of the ROV is depicted in Equation (3):

$$M\dot{v}_r + C(v_r)v_r + D(v_r)v_r + g(\eta) = \tau_T + \tau_D \tag{3}$$

$M \in \mathbb{R}^{6 \times 6}$, $C \in \mathbb{R}^{6 \times 6}$, $D \in \mathbb{R}^{6 \times 6}$, $g \in \mathbb{R}^6$, $\tau_T \in \mathbb{R}^6$, and $\tau_D \in \mathbb{R}^6$ represent the inertial matrix; the Coriolis and centripetal force matrix; the damping matrix; the restoring force matrix; the control force and moment vector; and the lumped disturbance vector under the nominal model, respectively. Among them, $\tau_D = \tau_F + \tau_E$. $\tau_F \in \mathbb{R}^6$ represents the disturbance vector caused by ocean currents. Since it is difficult to obtain an accurate model of the ROV, $\tau_E \in \mathbb{R}^6$ represents the system model uncertainty caused by umbilical cables,

etc., which is the error between the accurate model and the nominal model. $\boldsymbol{\tau}_F$ is given by calculating Equation (4):

$$\boldsymbol{\tau}_F = -\boldsymbol{M}_{RB}\dot{\boldsymbol{v}}_c - \boldsymbol{C}_{RB}(\boldsymbol{v}_r + \boldsymbol{v}_c)\boldsymbol{v}_c - \boldsymbol{C}_{RB}(\boldsymbol{v}_c)\boldsymbol{v}_r \tag{4}$$

where $\boldsymbol{M}_{RB} \in \boldsymbol{R}^{6\times6}$ represents the rigid-body inertia matrix and $\boldsymbol{C}_{RB} \in \mathbb{R}^{6\times6}$ represents the rigid-body Coriolis force and centripetal force matrix.

Assumption 2. *The lumped disturbance $\boldsymbol{\tau}_D$ and its derivative $\dot{\boldsymbol{\tau}}_D$ satisfy the bounded condition $\|\boldsymbol{\tau}_D\|_2 \le k_D$, $\|\dot{\boldsymbol{\tau}}_D\|_2 \le k_{dD}$, where k_D and k_{dD} are definite constants.*

2.3. Distribution of Thrust Forces

The operational ROV studied in this paper is equipped with four horizontal thrusters and four vertical thrusters. The distribution relationship between the control force and moment $\boldsymbol{\tau}_T$ and the thrust of each thruster is

$$\boldsymbol{\tau}_T = \boldsymbol{BU}, \tag{5}$$

where $\boldsymbol{U} \in \mathbb{R}^8$ represents the thrust vector generated by the thruster and $\boldsymbol{B} \in \mathbb{R}^{6\times8}$ represents the ROV thrust distribution matrix. The thrusters can provide a thrust range of ±4000 N.

2.4. Control Objectives

The control objectives of this paper are to design a high-precision motion control scheme for an operational ROV that is affected by ocean current disturbance and cannot obtain an accurate model. The aim is to enable the ROV to achieve precise positioning and docking with the underwater tool platform. Due to the structural requirements of the underwater tool platform, the positioning error of the ROV should be less than 0.05 m, and the error of each attitude angle should be less than $1°$.

3. Model-Assisted Finite-Time Sliding-Mode Extended State Observer

This section provides a detailed description and proof of the model-assisted finite-time sliding-mode extended state observer. First, the operational ROV nominal model is integrated into the extended state observer. The known model information can reduce the computational burden of the extended state observer and improve the estimation accuracy of disturbance and uncertainty. At the same time, sliding-mode technology is introduced to further enhance the robustness and convergence velocity of the observer.

3.1. Design of MFSESO

From the above discussion on modeling the kinematics and dynamics of the operational ROV, it can be seen that the ocean current velocity v_f and the lumped disturbance $\boldsymbol{\tau}_D$ are unknown disturbance quantities that need to be estimated. Therefore, these two variables are set as the extended state variables of the system, and the ROV extended state equation is established as follows:

$$\begin{cases} \dot{\boldsymbol{x}}_1 = \boldsymbol{x}_2 + \boldsymbol{f}_1(\boldsymbol{x}_1) + \boldsymbol{h}\boldsymbol{u}(t) \\ \dot{\boldsymbol{x}}_2 = \dot{\boldsymbol{x}}_2 \\ \boldsymbol{y} = \boldsymbol{x}_1 \end{cases} \tag{6}$$

In Equation (6), $\boldsymbol{x} = \left[\boldsymbol{x}_1^T, \boldsymbol{x}_2^T\right]^T \in \mathbb{R}^{24}$. $\boldsymbol{x}_1 = \left[\boldsymbol{\eta}^T, \boldsymbol{v}_r^T\right]^T \in \mathbb{R}^{12}$ represents the state vector of the system, which can be measured with sensors; $\boldsymbol{x}_2 = \left[\boldsymbol{v}_f^T, \boldsymbol{\tau}_{MD}^T\right]^T \in \mathbb{R}^{12}$ represents the extended state vector of the system, which needs to be estimated using the observer. The lump-like disturbance vector $\boldsymbol{\tau}_{MD} = \boldsymbol{M}^{-1}\boldsymbol{\tau}_D \in \mathbb{R}^6$. $\boldsymbol{f}_1(\boldsymbol{x}_1) = \left[\boldsymbol{J}(\boldsymbol{\eta})\boldsymbol{v}_r, -\boldsymbol{M}^{-1}\boldsymbol{f}(\boldsymbol{v}_r, \boldsymbol{\eta})\right]^T \in \mathbb{R}^{12}$ is the known function vector of the system, where $\boldsymbol{f}(\boldsymbol{v}_r, \boldsymbol{\eta}) = \boldsymbol{C}(\boldsymbol{v}_r)\boldsymbol{v}_r + \boldsymbol{D}(\boldsymbol{v}_r)\boldsymbol{v}_r +$

$g(\eta) \in \mathbb{R}^6$. $h = \left[0_{6 \times 6}, M^{-1}\right]^T \in \mathbb{R}^{12 \times 6}$ is the known function matrix of the system. $u(t) = \tau_T \in \mathbb{R}^6$ indicates the system control input and $y \in \mathbb{R}^{12}$ indicates the system output. According to the actual operational conditions of the ROV, it can be assumed that each element in the state vectors x_1 and x_2 of the system is bounded.

In order to estimate the ocean current velocity v_f and lumped disturbance τ_D, the equation for the model-assisted finite-time sliding-mode extended state observer is as follows:

$$\begin{cases} \dot{\hat{x}}_1 = \hat{x}_2 + f_1(x_1) + hu(t) + \omega\iota_1(x_1 - \hat{x}_1) + \kappa_1|x_1 - \hat{x}_1|^{\frac{p}{q}}\operatorname{sgn}(x_1 - \hat{x}_1) \\ \dot{\hat{x}}_2 = \omega^2\iota_2(x_1 - \hat{x}_1) + \omega\kappa_2|x_1 - \hat{x}_1|^{\frac{p}{q}}\operatorname{sgn}(x_1 - \hat{x}_1) \end{cases} \tag{7}$$

In Equation (7), $\hat{x} = \left[\hat{x}_1^T, \hat{x}_2^T\right]^T \in \mathbb{R}^{24}$ represents the state variable of MFSESO, which estimates the state variable x, where $\hat{x}_1 = \left[\hat{\eta}^T, \hat{v}_r^T\right]^T \in \mathbb{R}^{12}$, $\hat{x}_2 = \left[\hat{v}_f^T, \hat{\tau}_{MD}^T\right]^T \in \mathbb{R}^{12}$, and $\hat{\tau}_D = M\hat{\tau}_{MD} \in \mathbb{R}^6$. ω is the observer scale parameter; ι_1 and ι_2 are the observer gain parameters; and κ_1 and κ_2 are the observer sliding-mode gain parameters, both of which are definite positive real numbers. sgn represents the sign function, and p and q are the observer quasi-sliding-mode parameters, both of which are positive odd numbers, and $p < q$. In the aforementioned parameters, the correlation between $\hat{x}_1$ and $\hat{x}_2$ can be modified through the adjustment of ω. By selecting appropriate values for ι_1 and ι_2, the poles of the MFSESO characteristic equation can be determined, thereby affecting the convergence performance of the observer. κ_1 and κ_2 enhance the robustness of the observer. At the same time, $|x_1 - \hat{x}_1|^{\frac{p}{q}}\operatorname{sgn}(x_1 - \hat{x}_1)$ replaces the traditional sign function, effectively reducing the chattering phenomenon of sliding mode control.

3.2. Convergence Analysis of MFSESO

Theorem 1. *For the ROV extended state equation established above in Equation (6), the observation error of MFSESO designed in Equation (7) can converge to zero in finite time.*

The observation error state equation can be obtained by differentiating the system's extended state equation in Equation (6) and the MFSESO equation in Equation (7), as shown in Equation (8):

$$\begin{bmatrix} \dot{e}_1 \\ \dot{e}_2 \end{bmatrix} = \begin{bmatrix} -\omega\iota_1 I_{12 \times 12} & \omega I_{12 \times 12} \\ -\omega\iota_2 I_{12 \times 12} & 0_{12 \times 12} \end{bmatrix}\begin{bmatrix} e_1 \\ e_2 \end{bmatrix} + \begin{bmatrix} 0_{12 \times 1} \\ \dot{x}_2/\omega \end{bmatrix} - \begin{bmatrix} \kappa_1|e_1|^{\frac{p}{q}}\operatorname{sgn}(e_1) \\ \kappa_2|e_1|^{\frac{p}{q}}\operatorname{sgn}(e_1) \end{bmatrix} \tag{8}$$

where $e = \left[e_1^T, e_2^T\right]^T \in \mathbb{R}^{24}$; $e_1 = x_1 - \hat{x}_1$ and $e_2 = \frac{x_2}{\omega} - \frac{\hat{x}_2}{\omega}$; $\overline{A} = \omega\begin{bmatrix} -\iota_1 I_{12 \times 12} & I_{12 \times 12} \\ -\iota_2 I_{12 \times 12} & 0_{12 \times 12} \end{bmatrix} \in \mathbb{R}^{24 \times 24}$; $\overline{D} = \begin{bmatrix} 0_{12 \times 1} \\ \dot{x}_2/\omega \end{bmatrix} \in \mathbb{R}^{24}$; and $\overline{B} = \begin{bmatrix} \kappa_1|e_1|^{\frac{p}{q}}\operatorname{sgn}(e_1) \\ \kappa_2|e_1|^{\frac{p}{q}}\operatorname{sgn}(e_1) \end{bmatrix} \in \mathbb{R}^{24}$. When the observer gain parameters ι_1 and ι_2 satisfy $\iota_1^2 - 4\iota_2 > 0$, all eigenvalues of $\overline{A}$ have a negative real part. That is, $\overline{A}$ is the Hurwitz matrix.

Lemma 1 (Lyapunov Matrix Equation). *If the matrix $\overline{A}$ is a Hurwitz matrix, then for any given symmetric positive definite matrix $Q \in \mathbb{R}^{24 \times 24}$, there exists a symmetric positive definite matrix $P \in \mathbb{R}^{24 \times 24}$, such that $\overline{A}^T P + P\overline{A} = -Q$ is satisfied.*

To facilitate calculation, $Q = I$ is selected, matrix $\overline{A}$ is brought into Lemma 1, and P satisfying the condition is calculated:

$$P = \begin{bmatrix} P_{11} & P_{12} \\ P_{21} & P_{22} \end{bmatrix} = \begin{bmatrix} \frac{1}{2\omega}\frac{\iota_2+1}{\iota_1}I_{12 \times 12} & -\frac{1}{2\omega}I_{12 \times 12} \\ -\frac{1}{2\omega}I_{12 \times 12} & \frac{1}{2\omega}\frac{\iota_1^2+\iota_2+1}{\iota_1\iota_2}I_{12 \times 12} \end{bmatrix} \tag{9}$$

From the above, $\|P\|_F = \frac{\sqrt{3}}{\omega}\left[\left(\frac{\iota_2+1}{\iota_1}\right)^2 + \left(\frac{\iota_1^2+\iota_2+1}{\iota_1\iota_2}\right)^2 + 2\right]^{\frac{1}{2}}$; $\|\cdot\|_F$ is the Fibonacci norm.

To prove the convergence of the MFSESO system, the Lyapunov function of the system is chosen:

$$V = e^T P e. \tag{10}$$

Taking the derivative of the Lyapunov function V,

$$\dot{V} = e^T P \dot{e} + \dot{e}^T P e. \tag{11}$$

Substituting Equation (8) into Equation (11) yields the following:

$$\begin{aligned}
\dot{V} &= e^T\left(P\overline{A} + \overline{A}^T P\right)e + 2e^T P\overline{D} - 2e^T P\overline{B} \\
&= -\|e\|_2^2 + 2e^T P\overline{D} - 2e^T P\overline{B}
\end{aligned} \tag{12}$$

According to Assumption 1 and Assumption 2, it can be seen that $\left\|\dot{v}_f\right\|_2 \le k_{df}$ and $\left\|\dot{\tau}_{MD}\right\|_2 \le \left\|M^{-1}\right\|_F\|\dot{\tau}_D\|_2 \le k_{dD}\left\|M^{-1}\right\|_F$. Therefore, when $\|\overline{D}\|_2 \le \left\|\begin{matrix}k_{df}\\k_{dD}\left\|M^{-1}\right\|_F\end{matrix}\right\|_2/\omega = M_D$, we obtain the following:

$$2e^T P\overline{D} \le 2M_D\|P\|_F\|e\|_2. \tag{13}$$

Meanwhile, since P is a symmetric positive definite matrix, there is an orthogonal matrix $O \in \mathbb{R}^{24\times24}$, so that $O^T P O = \Lambda \in \mathbb{R}^{24\times24}$ is a diagonal matrix; thus, we can obtain Equation (14):

$$\begin{aligned}
2e^T P\overline{B} &= 2e^T O^T \Lambda O\overline{B} \\
&= 2(Oe)^T \Lambda(O\overline{B}) \\
&\ge 2\lambda_{\min}\min\{\kappa_1,\kappa_2\}\left(\sum_{i=1}^{24}\left(e_i|e_i|^{\frac{p}{q}}\operatorname{sgn}(e_i)\right)\right) \\
&\ge 2\lambda_{\min}\min\{\kappa_1,\kappa_2\}\left(\sum_{i=1}^{24}|e_i|^{\frac{q+p}{q}}\right) \\
&= 2\lambda_{\min}\min\{\kappa_1,\kappa_2\}\|e\|_{(q+p)/q}^{(q+p)/q} \\
&\ge 2\alpha\lambda_{\min}\min\{\kappa_1,\kappa_2\}\|e\|_2^{(q+p)/q}
\end{aligned}, \tag{14}$$

where $\|\cdot\|_{(q+p)/q}$ is the p-norm with exponent $(q+p)/q$, and $\lambda_{\min} = \frac{l_1^2+(l_2+1)^2-\sqrt{\left[l_1^2+(l_2+1)^2\right]\left[l_1^2+(l_2-1)^2\right]}}{4\omega l_1 l_2}$ is the minimum eigenvalue of P. Due to the equivalence of vector norms, there exists $\|e\|_{(q+p)/q}^{(q+p)/q} \ge \alpha\|e\|_2^{(q+p)/q}$, $\alpha > 0$. If we let $M_B = 2\alpha\lambda_{\min}\min\{\kappa_1,\kappa_2\}$, then $-2e^T P\overline{B} \le -M_B\|e\|_2^{(q+p)/q}$. To sum up, Equation (15) can be obtained:

$$\dot{V} \le -\|e\|_2^2 - M_B\|e\|_2^{(q+p)/q} + 2M_D\|P\|_F\|e\|_2 \tag{15}$$

Lemma 2 ([29]). *Consider the following nonlinear systems:*

$$\dot{x} = f(x), \tag{16}$$

where $f(0) = 0$, $x \in \mathbb{R}^n$, $f : U_0 \to \mathbb{R}^n$ is a continuous function in an open neighborhood U_0 containing the origin. Suppose there is a continuous positive definite function $V(x) : U_0 \to \mathbb{R}^n$, and that there are real numbers $a, b, c > 0$ and $d \in (0.5, 1)$, and an open neighborhood $\hat{U} \subseteq U_0$ containing the origin, such that the following equation holds:

$$\dot{V} \leq -aV^d - bV + cV^{\frac{1}{2}}. \tag{17}$$

Then, the origin of the system in Equation (16) is in fast finite time, uniformly bounded, stable. This implies that x converges to a stable region $Q = \left\{ x : \chi V^{d-\frac{1}{2}} + \delta V^{\frac{1}{2}} < c \right\}$, $\chi \in (0, a)$, $\delta \in (0, b)$. And the stable time T depends on the initial value $x(0)$, satisfying $T \leq \frac{1}{(b-\delta)(1-d)} \ln\left(1 + \frac{(b-\delta)V_{x(0)}^{1-d}}{a-\chi} \right)$.

The following can be seen from Equation (10):

$$\lambda_{\min} \|e\|_2^2 \leq V \leq \|P\|_F \|e\|_2^2. \tag{18}$$

According to Equations (15) and (18), we obtain

$$\begin{aligned} \dot{V} &\leq -M_B \|P\|_F^{-\frac{q+p}{2q}} V^{\frac{q+p}{2q}} - \|P\|_F^{-1} V + 2M_D \lambda_{\min}^{-\frac{1}{2}} \|P\|_F V^{\frac{1}{2}} \\ &= -a_0 V^{d_0} - b_0 V + c_0 V^{\frac{1}{2}} \end{aligned}, \tag{19}$$

where $a_0 = M_B \|P\|_F^{-\frac{q+p}{2q}}$, $b_0 = \|P\|_F^{-1}$, $c_0 = 2M_D \lambda_{\min}^{-\frac{1}{2}} \|P\|_F$, and $d_0 = \frac{q+p}{2q}$. According to Lemma (2), it can be seen that the observation error e can converge to the stable region $Q_0 = \left\{ e : \chi_0 V^{d_0 - \frac{1}{2}} + \delta_0 V^{\frac{1}{2}} < c_0 \right\}$, $\chi_0 \in (0, a_0)$, $\delta_0 \in (0, b_0)$ in a finite time. And the convergence time satisfies $T \leq \frac{1}{(b_0 - \delta_0)(1 - d_0)} \ln\left(1 + \frac{(b_0 - \delta_0)V_{e(0)}^{1-d_0}}{a_0 - \chi_0} \right)$, where the value of e at time $t = 0$ is defined as $e(0)$.

The above proves that the observation error e of MFSESO can converge to the stable region within $t = T$ time, indicating that MFSESO can achieve finite-time estimation of velocity disturbance v_f and lumped disturbance τ_D. This completes the proof of Theorem 1.

4. Double Closed-Loop Fractional-Order PI$^\lambda$D$^\mu$ Controller

It can be seen from the previous discussion that ocean current velocity v_f is mainly reflected in the ROV kinematic model and is not in the same channel as the system control input τ_T, which belongs to non-matching disturbance. The lumped disturbance τ_E acts on the dynamic model and belongs to the matching disturbance. It is difficult to directly offset the influence of non-matching disturbance simply with the input τ_T in the dynamic model. A double closed-loop controller should be designed to compensate for the disturbance of ocean current velocity v_f in the position loop and the disturbance of lumped disturbance τ_E in the velocity loop. A fractional-order PI$^\lambda$D$^\mu$ controller not only preserves the advantages of the simplicity, practicality, and easy tuning of the traditional PID controller, but also effectively enhances the robustness and dynamic capability of a dynamic system. So, the fractional-order PI$^\lambda$D$^\mu$ controller is introduced into the velocity loop control.

Design of DFOPID

The commonly used definitions of fractional calculus are the Riemann–Lioucille definition, the Grunwald Letnikov definition, and the Caputo definition [19]. The Riemann–Lioucille definition and the Grunwald Letnikov definition require the value of the fractional derivative of the signal at the initial moment to be known, while the Caputo definition requires the value of the signal and its integer derivative at the initial moment to be known, which is closer to practical applications. Therefore, the double closed-loop fractional-order PI$^\lambda$D$^\mu$ controller designed in this paper adopts the Caputo definition, as follows:

For $\alpha \in \mathbb{R}^+$, with $m - 1 < \alpha \leq m$ and $m \in \mathbb{Z}^+$, the α-order Caputo fractional derivative of the function $y(t)$ defined on $[t_0, t]$ is

$$_{t_0}D_t^\alpha y(t) = \frac{1}{\Gamma(m-\alpha)}\int_{t_0}^t \frac{y^{(m)}(\tau)}{(t-\tau)^{1+\alpha-m}}d\tau. \tag{20}$$

For $\gamma \in \mathbb{R}^+$, the γ-order Caputo fractional integral of function $y(t)$ defined on $[t_0, t]$ is

$$_{t_0}D_t^{-\gamma}y(t) = \frac{1}{\Gamma(\gamma)}\int_{t_0}^t \frac{y(\tau)}{(t-\tau)^{1-\gamma}}d\tau. \tag{21}$$

Among them, the Gamma function $\Gamma(x)$ is defined as

$$\Gamma(x) = \int_0^\infty t^{x-1}e^{-t}dt. \tag{22}$$

The output expression of the fractional-order $PI^\lambda D^\mu$ controller in the time domain is

$$u(t) = k_p e(t) + k_{i0}D^{-\lambda}e(t) + k_{d0}D^\mu e(t), \tag{23}$$

where $e(t) = r(t) - y(t)$ is the system error signal, which serves as the input signal of the fractional-order $PI^\lambda D^\mu$ controller; $r(t)$ is the reference input signal of the system; and $y(t)$ is the actual input signal of the system. k_p, k_i, and k_d represent the proportional, integral, and differential gains, respectively. λ and μ represent fractional orders of the integral and differential terms, respectively. The ranges of these values are $0 < \lambda < 2$ and $0 < \mu < 2$, respectively. It can be seen from the above discussion that due to the presence of fractional-order operators, the fractional-order $PI^\lambda D^\mu$ controller can adjust the low- and high-frequency characteristics of the closed-loop system more flexibly by modifying the values of λ and μ. Simultaneously, they are less sensitive to the parameter changes in the control system. When the control parameters and disturbance vary within a certain interval, the system performance does not change significantly. The system has stronger robustness. Meanwhile, fractional $PI^\lambda D^\mu$ is an extension of integer PID, naturally inheriting the advantages of the simple structure and easy tuning of integer PID.

The position loop controller is primarily responsible for eliminating the non-matching disturbance caused by the ocean current velocity v_f and guiding the operational ROV to achieve a smooth transition process. The position loop controller designed in this paper incorporates a saturated nonlinear link at the input of the PID algorithm to facilitate the ROV in reaching the target position at an optimal velocity:

$$v_d(t) = k_{\eta p}\bar{e}_\eta(t) + k_{\eta i}\int_{t_0}^t \bar{e}_\eta(t)dt + k_{\eta d}\frac{d\bar{e}_\eta(t)}{dt}. \tag{24}$$

In Equation (24), $\bar{e}_\eta(i) = sat(e_\eta(i))$, $e_\eta(i) = \eta_d(i) - \eta(i)$, and $i = 1, \ldots, 6$, where η_d is the desired position, $sat(e_\eta(i)) = \begin{cases} \Delta(i), e_\eta(i) > \Delta(i) \\ e_\eta(i), |e_\eta(i)| \le \Delta(i) \\ -\Delta(i), e_\eta(i) < -\Delta(i) \end{cases}$, $\Delta \in \mathbb{R}^6$ is the boundary-layer vector, and $k_{\eta j} \in \mathbb{R}^{6\times6}$, $j = p, i, d$ is the control gain diagonal matrix.

Due to the increased demands of ROV dynamics for control robustness and dynamic performance, a fractional-order $PI^\lambda D^\mu$ controller is designed to serve as the velocity loop controller:

$$\tau_c(t) = k_{vp}e_v(t) + k_{vi0}D^{-\lambda_v}e_v(t) + k_{vd0}D^{\mu_v}e_v(t). \tag{25}$$

In Equation (25), $e_v = v_d - v_r - \hat{v}_c \in \mathbb{R}^6$, $\hat{v}_c = J^{-1}(\eta)\hat{v}_f$, where v_d is desired velocity, $k_{vj} \in \mathbb{R}^{6\times6}$, $j = p, i, d$ is the control gain diagonal matrix, and $_0D^{i_v}e_j(t) \in \mathbb{R}^{6\times6}$, $i = -\lambda, \mu$ is the fractional calculus diagonal matrix.

The FADRC scheme developed for the ROV to perform high-precision positioning and docking control tasks is illustrated in Figure 2. The FADRC scheme, outlined with a red chain line in the figure, consists of DFOPID and MFSESO. DFOPID comprises a position

loop controller and a velocity loop controller. The position loop controller utilizes the position error η to generate the desired velocity v_d. The velocity error e_v is obtained by subtracting the ROV velocity v_r and the ocean current velocity observation $\hat{v}_c$ from the desired velocity v_d. The velocity loop controller determines the DFOPID controller output τ_C based on the velocity error e_v. MFSESO, based on inputs such as the ROV position η, the ROV velocity v_r, and the FADRC scheme output τ_T, calculates the ocean current velocity observation $\hat{v}_f$ and the lumped disturbance observation $\hat{\tau}_D$. The FADRC scheme output τ_T is derived from the disparity between the DFOPID controller output τ_C and the lumped disturbance observation $\hat{\tau}_D$. In summary, the FADRC scheme incorporates the ocean current velocity observation value $\hat{v}_f$ and the lumped disturbance observation value $\hat{\tau}_D$ estimated by MFSESO into the double closed-loop controller, so that the non-matching disturbance is transformed into matching disturbance, making it easier to mitigate their impact. During the transition process, DFOPID ensures accurate and rapid tracking of the ROV's position and velocity in relation to the target value. This enhances the robustness and dynamic characteristics of the entire system.
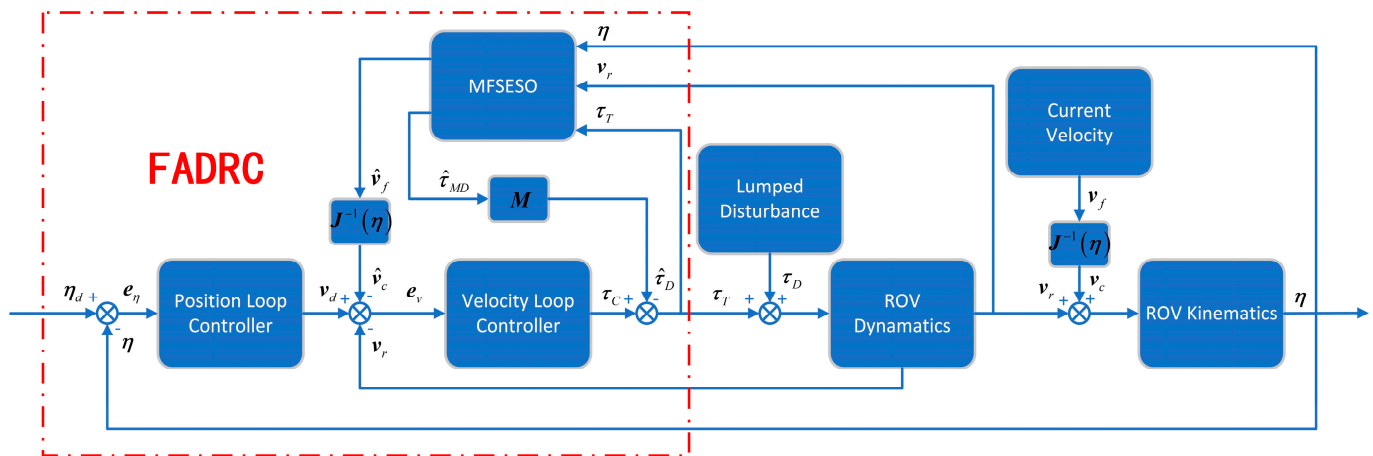
Figure 2. FADRC structural framework. FADRC consists of DFOPID and MFSESO, which is the part outlined with the red chain line. Desired position η_d (defined in line 373); ROV position η (defined in line 195); position error e_η (defined in line 373); velocity error e_v (defined in line 379); desired velocity v_d (defined in line 379); ROV velocity v_r (defined in line 202) under the body coordinate system {B}; ocean current velocity v_c (defined in line 207) and velocity observation $\hat{v}_c$ (defined in line 379) under the body coordinate system {B}; ocean current velocity v_f (defined in line 204) and velocity observation $\hat{v}_f$ (defined in line 271) under the inertial coordinate system {I}; lumped disturbance τ_D (defined in line 220) and lumped disturbance observation $\hat{\tau}_D$ (defined in line 272); lump-like disturbance τ_{MD} (defined in line 262) and lump-like disturbance observation $\hat{\tau}_{MD}$ (defined in line 272); DFOPID controller output τ_C (defined in line 378); FADRC scheme output τ_T (defined in line 222); inertial matrix M (defined in line 220); velocity transformation matrix $J(\eta)$ (defined in line 201).

5. Numerical Simulations and Pool Experiments

In order to verify the effectiveness and advanced nature of the control scheme proposed in this paper, high-precision ROV positioning and docking control experiments were conducted in both simulation and pool environments. Meanwhile, a comparison was carried out using the most widely used traditional method. The high-precision positioning and docking process of the ROV was as follows: In the ocean current environment with a flow velocity of 1 knot, the ROV was guided to the docking position using the visual positioning system and maintained its dynamic position. When the positioning error continued to remain within the required error range for docking, the docking locking mechanism extended downward into the docking hole of the underwater tool platform to complete the docking process.

5.1. ROV Prototype

As shown in Figure 3a, the ROV in this paper has an overall size of 3100 mm $\times$ 2000 mm $\times$ 1800 mm and a net weight of 4187.5 kg. It is equipped with four horizontal thrusters and four vertical thrusters, and has an omnidirectional driving capability. The bottom protruding part is equipped with two docking rods, which can perform docking operations with docking holes on the underwater tool platform. The parameters of the ROV nominal dynamic model are as follows: the center of gravity coordinate $r_G = [0, 0, 0]^T$, the center of buoyancy coordinate $r_B = [0, 0, -0.493]^T$, the moment of inertia matrix $I = diag(2038, 3587, 3587)$, the additional mass matrix $M_{AM} = -diag(3261.35, 4664.31, 7471.75, 1664, 4118.17, 3708.41)$, the linear damping matrix $D_L = -diag(3610.00, 2462.99, 4566.59, 9810.00, 5220.90, 5841.54)$, the nonlinear damping matrix $D_N = -diag(952|u|, 2442.78|v|, 530.46|w|, 890|p|, 1876|q|, 2085.52|r|)$. As shown in Figure 3b, the underwater tool platform is equipped with various operational tools and a sampling basket necessary for the ROV. Once the ROV dives, it can complete various tasks by changing tools on the tool platform, significantly enhancing the working efficiency. The ROV determines the relative position by identifying the QR code affixed to the tool platform. The tool platform is designed with two central docking holes that work in conjunction with two docking rods to complete the docking operation. According to the design of the docking rods and docking holes, the ROV position error must be less than 0.05 m, and the attitude angle error must be less than $1°$.

(**a**)

(**b**)
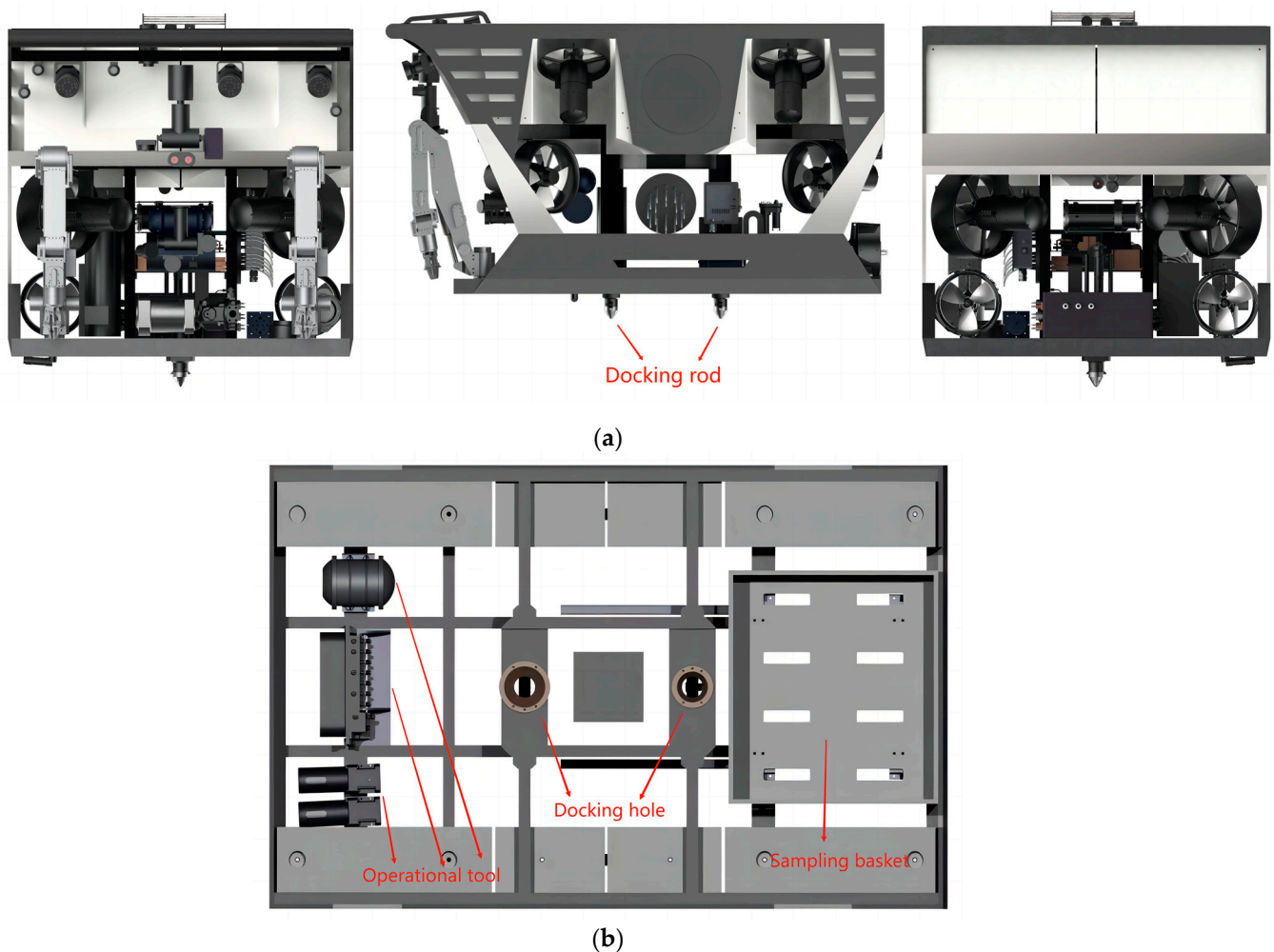
Figure 3. ROV and underwater tool platform structure diagrams. (**a**) ROV structure diagram: front view (left), left view (middle), and rear view (right). (**b**) Underwater tool platform structure diagram.

5.2. Numerical Simulations

In the numerical simulations, the position of the underwater tool platform was set to $\boldsymbol{\eta}_d = [5, 1, 1, 0, 0, 0]^T$. The initial position of the ROV was set to $\boldsymbol{\eta}(0) = [0, 0, 0, 0, 0, 0]^T$ and the initial velocity was set to $\boldsymbol{v}_r(0) = [0, 0, 0, 0, 0, 0]^T$. The ocean current velocity was set to $\boldsymbol{v}_f = [0.3635 \sin(0.05t + \pi/3), 0.3635 \sin(0.05t + \pi/3), 0, 0, 0, 0]^T$, simulating the actual operating conditions of 1 throttling. The disturbance caused by factors other than ocean current such as umbilical cable and the uncertainty of the system model were set to $\boldsymbol{\tau}_E =$

$$\begin{bmatrix} 10 \cos(0.05t + \pi/3) \sin(0.05t) \\ 10 \cos(0.05t + \pi/4) \cos(0.05t) \\ 10 \cos(0.05t + \pi/6) \sin(0.05t + \pi/4) \\ 2 \cos(0.05t + \pi/3) \cos(0.05t + \pi/10) \\ 2 \sin(0.05t) \sin(0.05t + 2\pi/3) \\ 2 \sin(0.05t + 4\pi/3) \cos(0.05t) \end{bmatrix}$$. The MFSESO observation parameters were set

to $\iota_1 = 10$, $\iota_2 = 10$, $\kappa_1 = 2$, and $\kappa_2 = 20$, $\omega = 1$, $p = 3$, $q = 5$. The DFOPID control parameters were set to $\boldsymbol{k}_{\eta p} = diag(1, 1, 1, 1, 1, 1)$, $\boldsymbol{k}_{\eta i} = diag(0, 0, 0, 0, 0, 0)$, $\boldsymbol{k}_{\eta d} = diag(0, 0, 0, 0, 0, 0)$, $\Delta = [0.5, 0.5, 0.5, \pi/180, \pi/180, \pi/180]^T$, $\boldsymbol{k}_{vp} = 100000 diag(1, 1, 1, 10, 10, 30)$, $\boldsymbol{k}_{vi} = diag(0.1, 0.1, 0.1, 0.1, 0.1, 0.1)$, $\boldsymbol{k}_{vd} = diag(10000, 50000, 50000, 0, 0, 0)$, $\boldsymbol{\lambda}_v = [1.1, 1.1, 1.1, 1.1, 1.1, 1.1]^T$ and $\boldsymbol{\mu}_\eta = [0.5, 0.5, 0.5, 0, 0, 0]^T$. An Oustaloup filter [30] was used to implement fractional calculus.

In order to further demonstrate the performance superiority of the FADRC scheme composed of MFSESO and DFOPID, the following simulation scenarios were conducted. The first scenario involved a comparison test between the control scheme based on MFSESO-DFOPID and the control scheme based on MFSESO-DPID. The second test scenario involved comparing the control scheme based on MFSESO-DFOPID with the control scheme based on LESO-DFOPID. The initial conditions of the test remained unchanged.

For simulation scenario 1, the high-precision positioning and docking control simulation results of the control scheme based on MFSESO-DFOPID and the control scheme based on MFSESO-DPID are shown in Figures 4 and 5.

Performance indicators such as the root-mean-square error, adjustment time, and steady-state error are presented in Table 1 to facilitate a more detailed and accurate quantitative comparison between the DFOPID algorithm and the DPID algorithm. Among them, a smaller root-mean-square error indicates that the scheme demonstrates a better control performance, while a shorter adjustment time signifies faster convergence, and the steady-state error reflects the accuracy of the control scheme.

Figure 4 illustrates the position error in the position loop and the velocity error in the velocity loop based on MFSESO-DFOPID and MFSESO-DPID. It can be seen from the figures that the position error and velocity error based on MFSESO-DFOPID show a better dynamic process, with a faster convergence velocity and smaller overshoot. At the same time, when the motion system is stabilized, MFSESO-DFOPID exhibits smaller position steady-state error and velocity steady-state error values. Meanwhile, against ocean current velocity disturbance and lumped disturbance, MFSEPO-DFOPID exhibits smaller error fluctuations and demonstrates greater robustness. Figure 5 shows the thrust curve of the thruster calculated using the schemes mentioned above, which remains generally smooth. This indicates that the control scheme proposed in this paper has good practical application value. The control performance indicators in Table 1 quantitatively support the results presented in Figure 4. MFSESO-DFOPID obviously meets the docking requirements, wherein the ROV position error must be less than 0.05 m and the attitude angle error must be less than 1°. MFSESO-DFOPID has a significant advantage in most indicators. The above results fully reflect that the DFOPID control algorithm proposed in this paper shows a better control performance than the traditional DPID algorithm. It exhibits a significantly improved dynamic response, reduced steady-state error, and enhanced robustness.

(**a**)

(**b**)
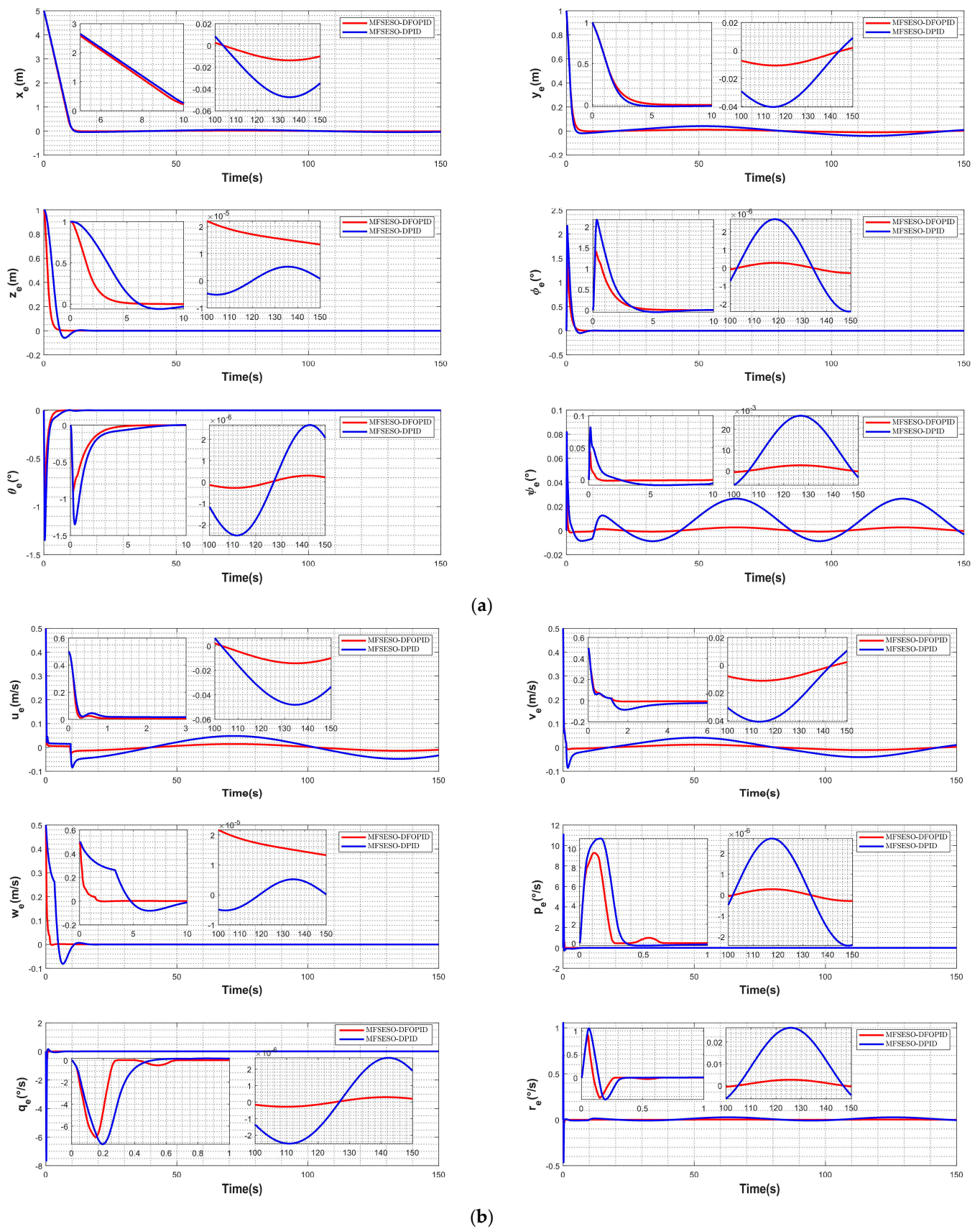
Figure 4. Position error e_η and velocity error e_v under MFSESO-DFOPID (red line) and MFSESO-DPID (blue line). (**a**) Position error e_η (defined in line 373). (**b**) Velocity error e_v (defined in line 379).
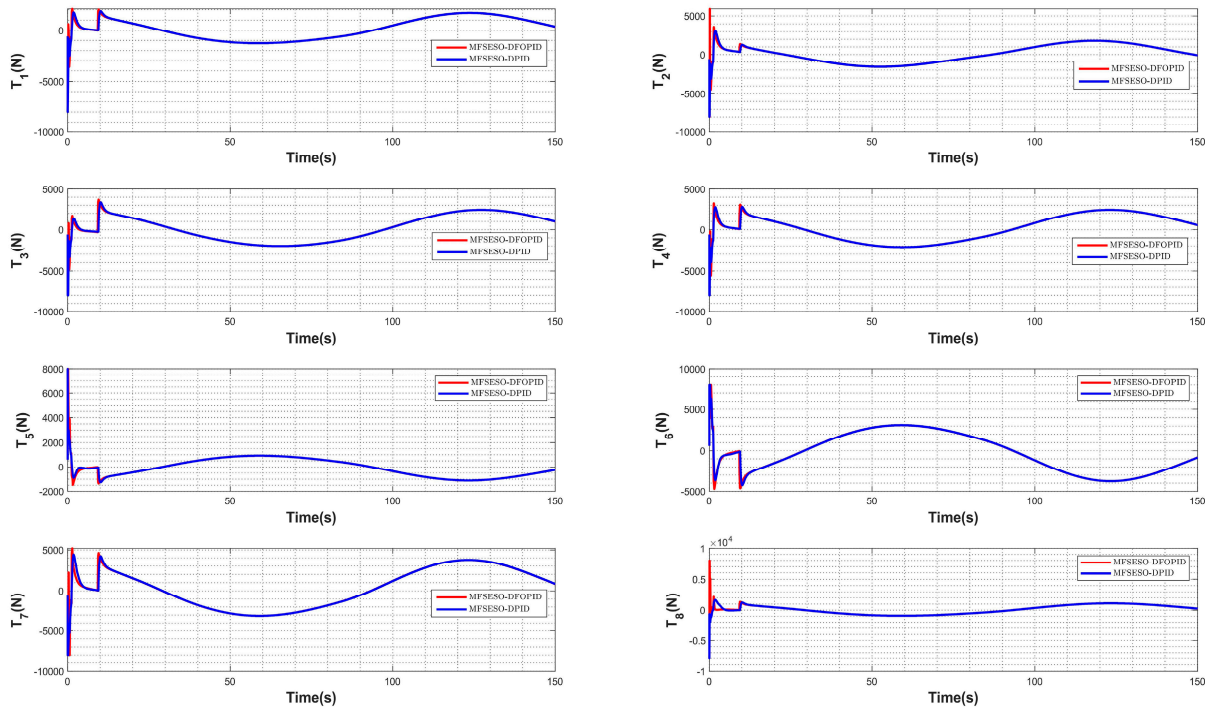
Figure 5. Thruster thrust U (defined in line 236) under MFSESO-DFOPID (red line) and MFSESO-DPID (blue line).

Table 1. Quantitative comparison between MFSESO-DFOPID and MFSESO-DPID control schemes. Better performance indicators are highlighted in red.

Performance Indicator	Control Scheme	x	y	z	ϕ	θ	ψ
Position root-mean-square error (m)	MFSESO-DFOPID	0.7606	0.0762	0.0833	0.0017	0.0010	3.36×10^{-5}
	MFSESO-DPID	0.7716	0.0789	0.1280	0.0028	0.0016	2.57×10^{-4}
Position adjustment time (s)	MFSESO-DFOPID	9.874	3.472	3.628	2.996	2.596	0.162
	MFSESO-DPID	10.030	2.836	5.610	3.118	3.310	0.668
Position steady-state error (m)	MFSESO-DFOPID	-0.0100	0.0019	1.34×10^{-5}	-2.86×10^{-7}	2.18×10^{-7}	-0.0003
	MFSESO-DPID	-0.0347	0.0090	6.78×10^{-7}	-2.41×10^{-6}	2.07×10^{-6}	-0.0032
Velocity root-mean-square error (m/s)	MFSESO-DFOPID	0.0167	0.0167	0.0179	0.0050	0.0033	2.86×10^{-4}
	MFSESO-DPID	0.0371	0.0308	0.0538	0.0067	0.0042	4.78×10^{-4}
Velocity adjustment time (s)	MFSESO-DFOPID	0.224	0.698	1.486	0.250	0.258	0.252
	MFSESO-DPID	12.542	2.916	9.256	0.330	0.422	0.318
Velocity steady-state error (m/s)	MFSESO-DFOPID	-0.0100	0.0022	1.32×10^{-5}	-2.86×10^{-7}	1.98×10^{-7}	-0.0005
	MFSESO-DPID	-0.0335	0.0105	1.66×10^{-7}	-2.39×10^{-6}	1.89×10^{-6}	-0.0045

For simulation scenario 2, the high-precision positioning and docking control simulation results of the control scheme based on MFSESO-DFOPID and the control scheme based on LESO-DFOPID are shown in Figure 6.

(**a**)

(**b**)
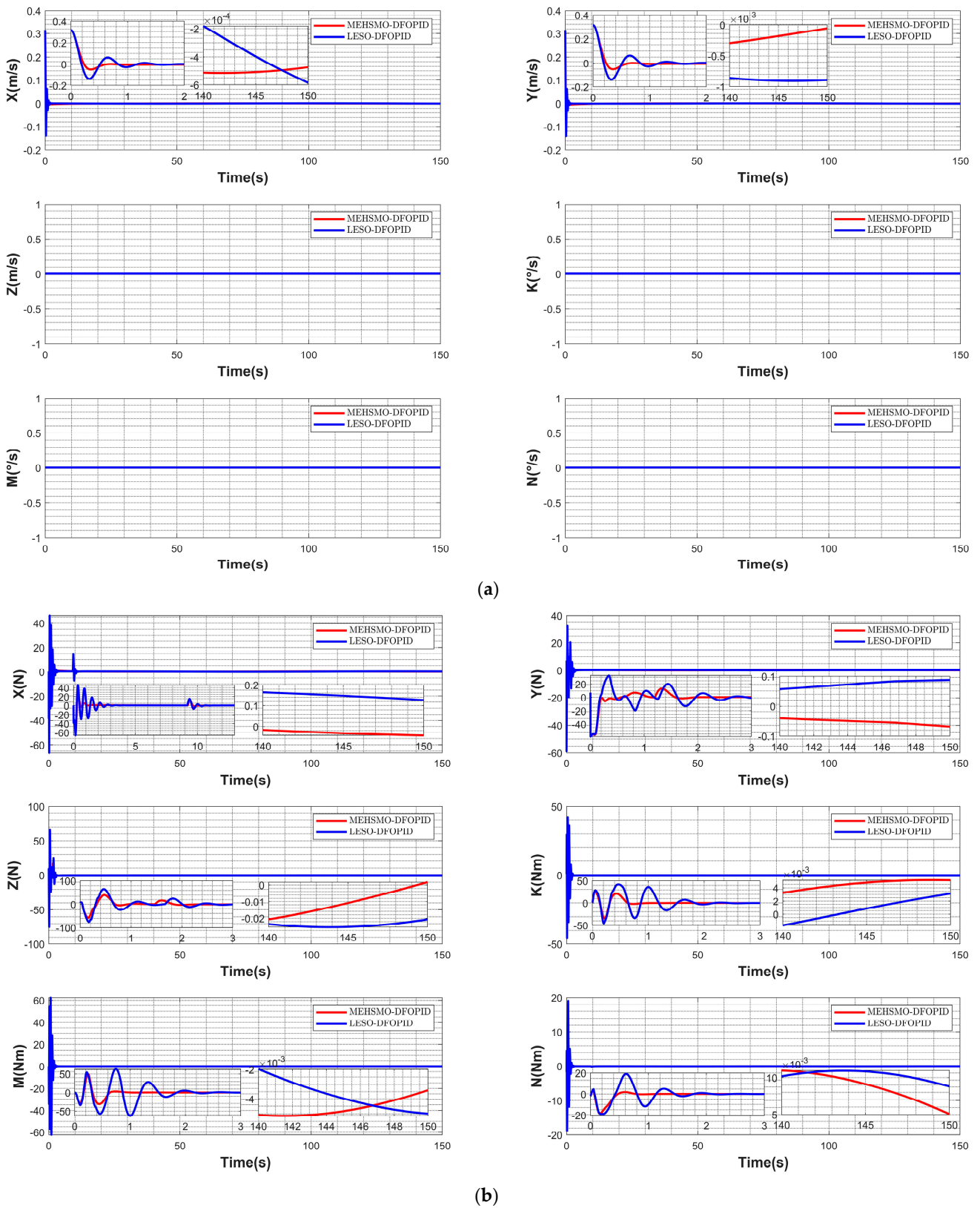
Figure 6. Observation error of ocean current velocity $\hat{v}_f$ and lumped disturbance $\hat{\tau}_D$ under MFSESO-DFOPID (red line) and LESO-DFOPID (blue line). (**a**) Observation error of ocean current velocity $\hat{v}_f$ (defined in line 271). (**b**) Observation error of lumped disturbance $\hat{\tau}_D$ (defined in line 272). Moreover, note that the six degrees of freedom for surge, sway, heave, roll, pitch, and yaw are represented by the letters X, Y, Z, K, M, and N, respectively.

In order to quantitatively compare the observation performance of the MFSESO and LESO algorithms for ocean current disturbance and lumped disturbance, performance indicators such as the root-mean-square error, adjustment time, and steady-state error are introduced in Table 2. The root-mean-square error of observation generally reflects the observation performance, the adjustment time of observation reflects the convergence velocity, and the steady-state error of observation reflects the estimation accuracy.

Table 2. Quantitative comparison between MFSESO-DFOPID and LESO-DFOPID control schemes. Better performance indicators are highlighted in red.

Performance Indicator	Control Scheme	x	y	z	ϕ	θ	ψ
Root-mean-square error of ocean current velocity observation (m/s)	MFSESO-DFOPID	0.0080	0.0080	0	0	0	0
	LESO-DFOPID	0.0091	0.0091	0	0	0	0
Adjustment time of ocean current velocity observation (s)	MFSESO-DFOPID	0.524	0.532	0	0	0	0
	LESO-DFOPID	1.078	1.082	0	0	0	0
Steady-state error of ocean current velocity observation (m/s)	MFSESO-DFOPID	-4.73×10^{-4}	-5.83×10^{-5}	0	0	0	0
	LESO-DFOPID	-5.86×10^{-4}	-8.95×10^{-4}	0	0	0	0
Root-mean-square error of lumped disturbance observation (N)	MFSESO-DFOPID	2.039	1.738	2.193	1.213	1.624	0.597
	LESO-DFOPID	2.953	2.119	3.320	2.517	3.720	1.031
Adjustment time of lumped disturbance observation (s)	MFSESO-DFOPID	10.002	1.888	3.334	0.912	0.942	0.738
	LESO-DFOPID	10.500	3.218	3.604	2.660	2.754	2.036
Steady-state error of lumped disturbance observation (N)	MFSESO-DFOPID	-0.043	0.0022	0.0016	0.0051	0.0034	0.0005
	LESO-DFOPID	0.126	0.0105	-0.0207	0.0031	-0.0050	0.0088

Figure 6a shows the estimation results for the MFSESO and LESO algorithms on ocean current velocity. It is not difficult to observe in the figure that, at X and Y degrees of freedom, MFSESO can approach the ocean current velocity more quickly, while the oscillation amplitude is smaller. With other degrees of freedom, the output of the observer remains 0 because no velocity disturbance is applied. Figure 6b shows the observation results for the MFSESO and LESO algorithms on lumped disturbance. It can be seen from this figure that the convergence process of MFSESO proposed in this paper is faster and smoother, and the steady-state error is smaller. The relevant performance indicators in Table 2 quantitatively describe the two observation algorithms, strongly demonstrating the significant advantages of MFSESO in terms of velocity, stability, and accuracy, and confirming the results in Figure 6. The above statement indicates that MFSESO can yield better observation results compared to the traditional LESO.

5.3. Pool Experiments

To verify the actual operational performance of the FADRC scheme based on MFSESO-DFOPID proposed in this article, a high-precision positioning and docking experiment using an ROV and a tool platform was conducted in a pool. The experimental scenario is depicted in Figure 7, the observation effect of the observer is reflected in Figures 8 and 9, and the position errors of each degree of freedom are illustrated in Figure 10.

As shown in Figure 7, the FADRC scheme based on MFSESO-DFOPID can enable the ROV to quickly and accurately reach the target position and complete the docking operation. Since the ROV is self-stabilized in pitch and roll degrees of freedom through the buoyancy trim, only four degrees of freedom x, y, z, ψ are controlled, where the total distance error $D = \sqrt{x_e{}^2 + y_e{}^2 + z_e{}^2}$. Figures 8 and 9 reflect that the observer in the control scheme effectively compensates for the current velocity disturbance and lumped disturbance at each degree of freedom. As can be seen from Figure 10, when $t > 20.40$ s, the position error $D < 0.05$ m, and when $t > 30.63$ s, the heading angle error $\psi < 1$. This proves that this control scheme can achieve high-precision positioning control and meet the requirements of docking control operations.

Figure 7. High-precision positioning and docking control experimental scenario. From top to bottom, the long image on the left contains frames 1–4, the middle long image includes frames 5–8, and the long image on the right includes frames 9–12. The entire positioning and docking process is clearly shown.
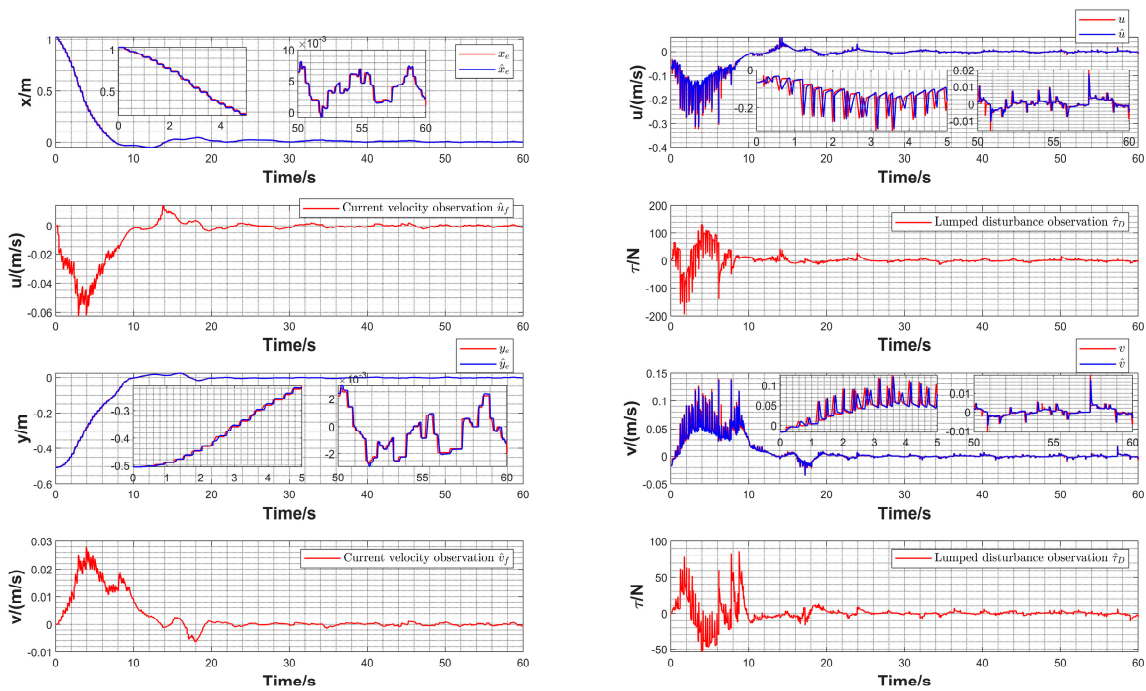
Figure 8. The x and y freedom observation results. Position x_e (red line) and position observation $\hat{x}_e$ (blue line); velocity u (red line) and velocity observation $\hat{u}$ (blue line); current velocity observation $\hat{u}_f$ (red line); lumped disturbance observation $\hat{\tau}_D$ (red line); position y_e (red line) and position observation $\hat{y}_e$ (blue line); velocity v (red line) and velocity observation $\hat{v}$ (blue line); current velocity observation $\hat{v}_f$ (red line); lumped disturbance observation $\hat{\tau}_D$ (red line).
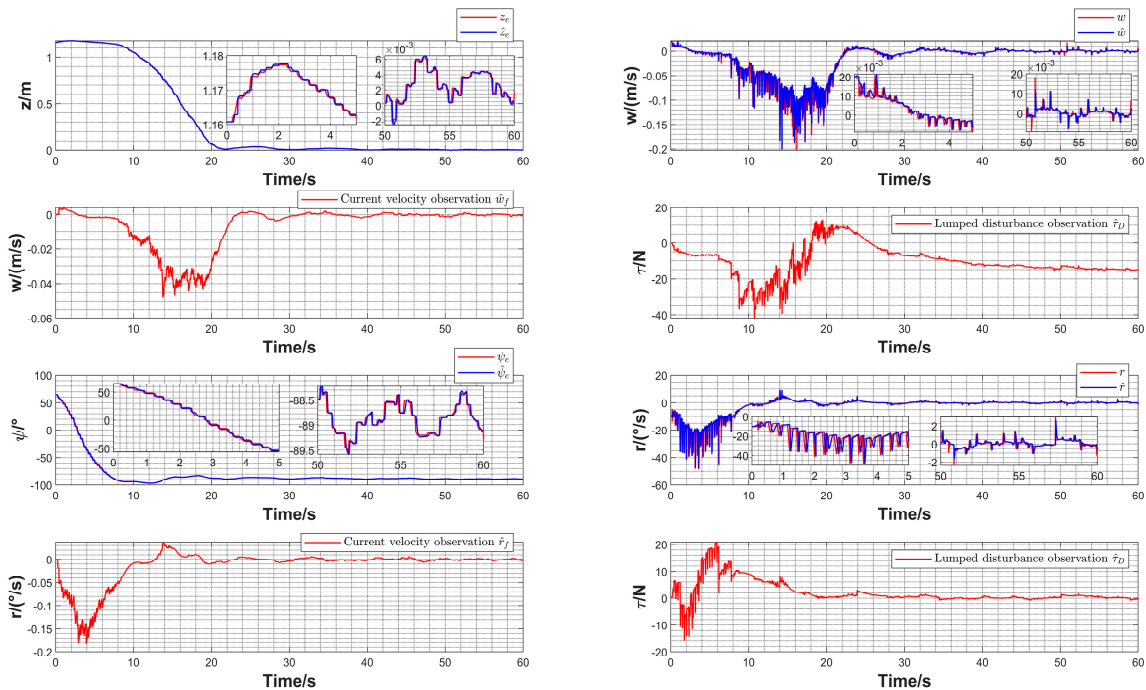
Figure 9. The z and ψ freedom observation results. Position z_e (red line) and position observation $\hat{z}_e$ (blue line); velocity w (red line) and velocity observation $\hat{w}$ (blue line); current velocity observation $\hat{w}_f$ (red line); lumped disturbance observation $\hat{\tau}_D$ (red line); orientation ψ_e (red line) and position observation $\hat{\psi}_e$ (blue line); velocity r (red line) and velocity observation $\hat{r}$ (blue line); current velocity observation $\hat{r}_f$ (red line); lumped disturbance observation $\hat{\tau}_D$ (red line).
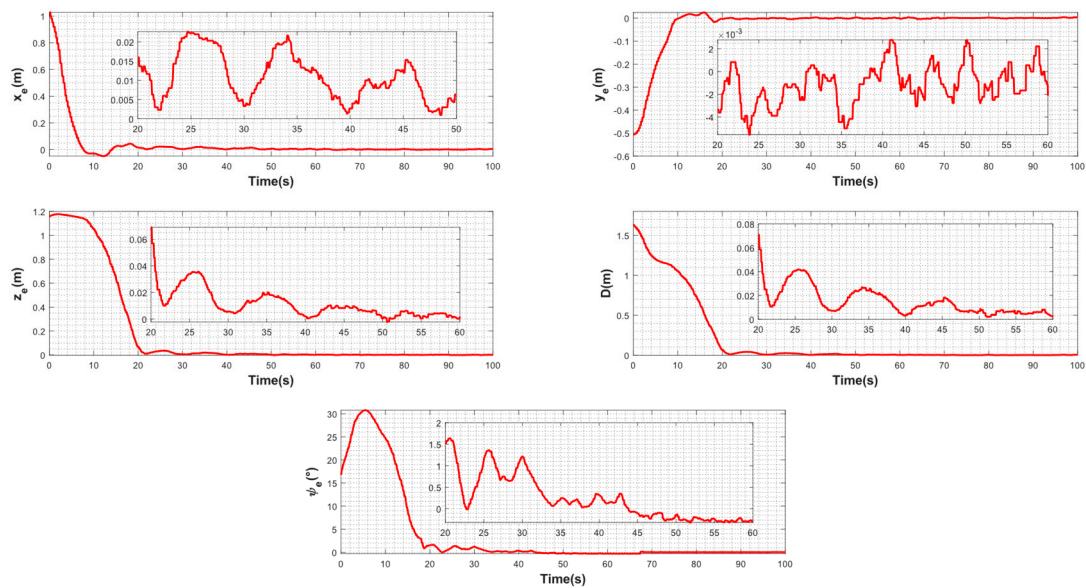
Figure 10. ROV position error. Position x_e (red line); position y_e (red line); position z_e (red line); total distance D (red line); and orientation ψ_e (red line).

6. Conclusions

In this study, an FADRC scheme is introduced, comprising a double closed-loop fractional-order $\mathrm{PI}^\lambda \mathrm{D}^\mu$ controller and a model-assisted finite-time sliding-mode extended state observer. The purpose of this control scheme is to facilitate high-precision positioning and docking tasks for ROVs in the presence of ocean current disturbances and model uncertainties. Specifically, DFOPID effectively addresses non-matched disturbances, with its fractional-order component enhancing the system's dynamic performance and robustness. The MFSESO in this paper further enhances the estimation accuracy by integrating sliding-mode technology and ensuring the finite-time convergence of observation errors. Through numerical simulations and pool experiments, it is demonstrated that the proposed control scheme can effectively mitigate ocean current disturbances and achieve high-precision operations even in the absence of an accurate model. This underscores the scheme's independence from precise model data on the operational ROV, while also highlighting benefits such as its simple structure and easy parameter tuning. Consequently, the FADRC scheme presented in this paper holds significant practical value and can serve as a valuable reference for ROVs engaged in high-precision operations. Future research will focus on exploring adaptive parameter optimization within the control scheme.

Author Contributions: Conceptualization, W.L. and L.G.; methodology, W.L. and L.G.; software, L.G.; validation, W.L. and J.X.; resources, W.L. and L.L.; writing—original draft preparation, L.G. and G.Y.; writing—review and editing, W.L. and L.L.; funding acquisition, W.L. All authors have read and agreed to the published version of the manuscript.

Data Availability Statement: The data presented in this study can be made available by sending a request to 2019100504@mail.nwpu.edu.cn.

Conflicts of Interest: The authors declare no conflicts of interest.

References

1. Makavita, C.D.; Jayasinghe, S.G.; Nguyen, H.D.; Ranmuthugala, D. Experimental Comparison of Two Composite MRAC Methods for UUV Operations with Low Adaptation Gains. *IEEE J. Oceanic. Eng.* **2020**, *45*, 227–246. [CrossRef]
2. Uchihori, H.; Cavanini, L.; Tasaki, M.; Majecki, P.; Yashiro, Y.; Grimble, M.J.; Yamamoto, I.; van der Molen, G.M.; Morinaga, A.; Eguchi, K. Linear Parameter-Varying Model Predictive Control of AUV for Docking Scenarios. *Appl. Sci.* **2021**, *11*, 4368. [CrossRef]
3. Ohrem, S.J.; Amundsen, H.B.; Caharija, W.; Holden, C. Robust adaptive backstepping DP control of ROVs. *Control Eng. Pract.* **2022**, *127*, 105282. [CrossRef]
4. Xie, T.; Li, Y.; Jiang, Y.; Pang, S.; Xu, X. Three-dimensional mobile docking control method of an underactuated autonomous underwater vehicle. *Ocean Eng.* **2022**, *265*, 112634. [CrossRef]
5. Wu, N.; Wang, M.; Ge, T.; Wu, C.; Yang, D.; Yang, R. Experiments on high-performance maneuvers control for a work-class 3000-m remote operated vehicle. *Proc. Inst. Mech. Eng. Part I J. Syst. Control Eng.* **2019**, *233*, 558–569. [CrossRef]
6. Song, D.; Li, L.; Wang, C.; Hou, R.; Li, C. A practical robust yaw servo architecture of ROVs by multi-vector propulsion and nonlinear controller. *Trans. Inst. Meas. Control* **2020**, *42*, 2908–2918. [CrossRef]
7. An, L.; Li, Y.; Cao, J.; Jiang, Y.; He, J.; Wu, H. Proximate time optimal for the heading control of underactuated autonomous underwater vehicle with input nonlinearities. *Appl. Ocean Res.* **2020**, *95*, 102002. [CrossRef]
8. Zhang, T.; Miao, X.; Li, Y.; Jia, L.; Wei, Z.; Gong, Q.; Wen, T. AUV 3D docking control using deep reinforcement learning. *Ocean Eng.* **2023**, *283*, 115021. [CrossRef]
9. Wang, T.; Sun, Z.; Ke, Y.; Li, C.; Hu, J. Two-Step Adaptive Control for Planar Type Docking of Autonomous Underwater Vehicle. *Mathematics* **2023**, *11*, 3467. [CrossRef]
10. Li, S.; Zhang, X. The welding tracking technology of an underwater welding robot based on sliding mode active disturbance rejection control. *Assem. Autom.* **2022**, *42*, 891–900. [CrossRef]
11. Han, J. From PID to Active Disturbance Rejection Control. *IEEE Trans. Ind. Electron.* **2009**, *56*, 900–906. [CrossRef]
12. Gao, Z. Active disturbance rejection control: From an enduring idea to an emerging technology. In Proceedings of the 10th International Workshop on Robot Motion and Control, Poznan University of Technology, Poznan, Poland, 1 July 2015; IEEE: Poznan, Poland, 2015; pp. 269–282.
13. Liu, C.; Xiang, X.; Yang, L.; Li, J.; Yang, S. A hierarchical disturbance rejection depth tracking control of underactuated AUV with experimental verification. *Ocean Eng.* **2022**, *264*, 112458. [CrossRef]
14. Wang, C.; Cai, W.; Lu, J.; Ding, X.; Yang, J. Design, Modeling, Control, and Experiments for Multiple AUVs Formation. *IEEE Trans. Autom. Sci. Eng.* **2021**, *19*, 2776–2787. [CrossRef]
15. Gao, J.; Liang, X.; Chen, Y.; Zhang, L.; Jia, S. Hierarchical image-based visual serving of underwater vehicle manipulator systems based on model predictive control and active disturbance rejection control. *Ocean Eng.* **2021**, *229*, 108814. [CrossRef]
16. Zhou, Y.; Sun, X.; Sang, H.; Yu, P. Robust dynamic heading tracking control for wave gliders. *Ocean Eng.* **2022**, *256*, 111510. [CrossRef]
17. Li, Z.; Liang, S.; Guo, M.; Zhang, H.; Wang, H.; Li, Z.; Li, H. ADRC-Based Underwater Navigation Control and Parameter Tuning of an Amphibious Multirotor Vehicle. *IEEE J. Oceanic. Eng.* **2024**, *13*, 4900. [CrossRef]
18. Liu, C.; Xiang, X.; Duan, Y.; Yang, L.; Yang, S. ADRC-SMC-based disturbance rejection depth-tracking control of underactuated AUV. *J. Field Robot.* **2024**, *41*, 1103–1115. [CrossRef]
19. Podlubny, I. Fractional-order systems and PID controllers. *IEEE Trans. Autom. Control* **1999**, *44*, 208–214. [CrossRef]
20. Liu, L.; Zhang, L.; Pan, G.; Zhang, S. Robust yaw control of autonomous underwater vehicle based on fractional-order PID controller. *Ocean Eng.* **2022**, *257*, 111493. [CrossRef]
21. Zhu, B.; Liu, L.; Zhang, L.; Liu, M.; Duanmu, Y.; Chen, Y.; Dang, P.; Li, J. A Variable-Order Fuzzy Logic Controller Design Method for an Unmanned Underwater Vehicle Based on NSGA-II. *Fractal Fract.* **2022**, *6*, 577. [CrossRef]
22. Li, Q.; Yang, G.; Yu, F.; Chen, Y. Adaptive fractional order non-singular terminal sliding mode controller for underwater soft crawling robots with parameter uncertainties and unknown disturbances. *Ocean Eng.* **2023**, *271*, 113728. [CrossRef]
23. Zhang, L.; Liu, L.; Zhang, S.; Cao, S. Saturation Based Nonlinear FOPD Motion Control Algorithm Design for Autonomous Underwater Vehicle. *Appl. Sci.* **2019**, *9*, 4958. [CrossRef]
24. Cui, Z.; Liu, L.; Zhu, B.; Zhang, L.; Yu, Y.; Zhao, Z.; Li, S.; Liu, M. Spiral Dive Control of Underactuated AUV Based on a Single-Input Fractional-Order Fuzzy Logic Controller. *Fractal Fract.* **2022**, *6*, 519. [CrossRef]
25. Liu, L.; Zhang, L.; Zhang, S. Robust PI controller design for AUV motion control withguaranteed frequency and time domain behaviour. *IET Control Theory A* **2021**, *15*, 784–792. [CrossRef]
26. Hasan, M.W.; Abbas, N.H. An adaptive neural network with nonlinear FOPID design of underwater robotic vehicle in the presence of disturbances, uncertainty, and obstacles. *Ocean Eng.* **2023**, *279*, 114451. [CrossRef]
27. Ali, N.; Tawiah, I.; Zhang, W. Finite-time extended state observer based nonsingular fast terminal sliding mode control of autonomous underwater vehicles. *Ocean Eng.* **2020**, *218*, 108179. [CrossRef]
28. Abdurahman, B.; Savvaris, A.; Tsourdos, A. Switching LOS guidance with speed allocation and vertical course control for path-following of unmanned underwater vehicles under ocean current disturbances. *Ocean Eng.* **2019**, *182*, 412–426. [CrossRef]

29.　Hu, Q.; Jiang, B. Continuous Finite-Time Attitude Control for Rigid Spacecraft Based on Angular Velocity Observer. *IEEE Trans. Aerosp. Electron. Syst.* **2018**, *54*, 1082–1092. [CrossRef]

30.　Oustaloup, A.; Levron, F.; Mathieu, B.; Nanot, F.M. Frequency-band complex noninteger differentiator: Characterization and synthesis. *IEEE Trans. Circuits Syst. I Fundam. Theory Appl.* **2000**, *47*, 25–39. [CrossRef]